Key Points:
- LOLA and radar data are compared to measure roughness at various length scales
- Radar roughness correlates well with 25–100 m scale topographic roughness
- The correlation is stronger at 70 cm radar wavelength than at 13 cm wavelength

Correspondence to:
E. R. Jawin,
Erica_Jawin@brown.edu

The relationship between radar scattering and surface roughness of lunar volcanic features

Erica R. Jawin[1,2,3], Walter S. Kiefer[2], Caleb I. Fassett[1], D. Benjamin J. Bussey[4], Joshua T. S. Cahill[4], M. Darby Dyar[1], Samuel J. Lawrence[5], and Paul D. Spudis[2]

[1]Department of Astronomy, Mount Holyoke College, South Hadley, Massachusetts, USA, [2]Lunar and Planetary Institute, Houston, Texas, USA, [3]Now at Department of Earth, Environmental, and Planetary Sciences, Brown University, Providence, Rhode Island, USA, [4]Johns Hopkins University Applied Physics Laboratory, Laurel, Maryland, USA, [5]School of Earth and Space Exploration, Arizona State University, Tempe, Arizona, USA

Abstract Lunar roughness measurements derived from the Lunar Orbiter Laser Altimeter are compared to 12.6 cm wavelength radar data collected by the Miniature Radio Frequency instrument and 70 cm wavelength radar data collected by the Arecibo Observatory. These data are compared to assess how surface and subsurface roughness are correlated and affected by parameters including age and composition at length scales between 0.1 and 100 m. A range of features are analyzed including volcanic domes (Marius Hills, Rümker Hills, Gruithuisen, and Mairan Domes); mare (Imbrium, Serenitatis, and Oceanus Procellarum); pyroclastic dark mantle deposits (Sinus Aestuum, Sulpicius Gallus, and Mare Vaporum); and two young craters (Copernicus and Tycho). Statistically significant positive correlations exist between topographic roughness and both P- and S-band circular polarization ratios. The strongest correlation is observed at the longest length scales. Correlations weaken as length scales become less similar, potentially due to distinct processes controlling surface modification. Roughness is not significantly correlated with local slope. Although the Marius Hills are compositionally distinct from the Gruithuisen and Mairan domes, they are indistinguishable in roughness characteristics. Conversely, the Rümker Hills, mare, and dark mantle deposits are smoother at the length scales examined, possibly due to fine-grained mantling of regolith or pyroclastic deposits. The floor and ejecta of Tycho are the roughest surfaces measured in this study, while the floor and ejecta of Copernicus overlap the roughness distribution of the volcanic features. This study shows that many factors control the evolution of roughness over time on various length scales.

1. Introduction

The physical characteristics of geologic features on the lunar surface are a function of their emplacement and modification history. For volcanic units in particular, the composition and mode of emplacement are important controls on the initial physical properties of the surface. Reworking of these units is then dominated by impactors of all sizes (from microns to kilometers), which leads to the breakdown of rocks [e.g., *Hörz et al.*, 1975], the growth of regolith [e.g., *Gault et al.*, 1966; *Quaide and Oberbeck*, 1975], and alteration of surface topography [e.g., *Soderblom*, 1970]. An observation that can be used to examine the resulting characteristics is surface roughness, which is a measure of the variation in topography over a defined length scale (see *Kreslavsky et al.* [2013] for a thorough description of roughness measurements).

In this study roughness characteristics of lunar volcanic and impact structures are examined using two types of data, laser altimetry and radar, in order to assess how surface and subsurface roughness are correlated, and how these are affected by various parameters, including emplacement mechanisms, composition, and age, which are unique to each geologic unit. It is expected that characteristics such as these may affect the erosional history of a feature in a unique manner. As such, characteristic roughnesses may allow one to identify and distinguish distinct features from these data.

Laser altimetry allows direct assessment of topographic surface roughness at a scale determined by the spacing between measurements [e.g., *Rosenburg et al.*, 2011; *Kreslavsky et al.*, 2013]. An additional metric of roughness can be derived from the laser altimeter at the scale of the measurement footprints, namely the variation received in pulse width travel time [e.g., *Neumann et al.*, 2003]. However, at present the relationship between surface roughness and beam spreading has not been completely calibrated for the LOLA altimeter [*Neumann et al.*, 2009; *Smith et al.*, 2010a]. Likewise, *Poole et al.* [2013] found that pulse width

data from LOLA only weakly correlated with surface roughness. For these reasons, pulse width observations have not been considered in detail here.

The radar properties of a surface are also sensitive to its roughness, which has proven useful for distinguishing geologic units of both terrestrial and planetary surfaces. For example, measurements taken of Kilauea volcano in Hawaii using the Space Shuttle Imaging Radar showed that volcanic flows of differing textures (a'a and pahoehoe), as well as pyroclastic ash deposits, were distinguishable at the L-band (23 cm wavelength) [*Gaddis et al.*, 1989, 1990]. Additionally, Earth-based P-band (70 cm) radar has allowed identification of rugged lava flows on the Moon, such as in Mare Serenitatis [*Campbell et al.*, 2009a], while S-band (12.6 cm) data were used to identify fine-grained pyroclastic deposits by their low backscatter and circular polarization ratio (CPR) values in Mare Vaporum and southern Mare Serenitatis [*Carter et al.*, 2009].

The radar waves used in these studies are circularly polarized and transmitted in one of the two possible polarizations. This polarization can be modified by the interaction of the radar wave with the Moon during either surface reflection or by subsurface volume scattering. The circular polarization ratio (CPR) provides a quantitative description of the change in polarization and is defined as the ratio of the radar echo in the same sense circular polarization to the echo in the opposite sense circular polarization. Geologically, CPR describes the amount of diffuse surface and volume scattering by features on the scale of the radar wavelength, or specular scattering from rock faces that are flat at the wavelength scale [e.g., *Campbell et al.*, 2009b; *Campbell*, 2012]. The scattering surface that causes a radar reflection can be either the surface of the Moon or a rock or interface that is buried at shallow depths in the regolith. Scattering off of buried structures is referred to as volume scattering; on the Moon, volume scattering is commonly thought to be due to rocks buried in the fine-grained regolith [see *Campbell et al.*, 2009b, Figure A1]. Just as rocks at the surface contribute to topographic roughness, rocks buried in the shallow subsurface are a type of volumetric textural roughness, and we will use the simple term roughness in this paper to refer to both surface and shallow subsurface roughness. When an incident beam reflects off an object or surface, it changes polarity to the opposite sense circular polarization (OC) of that transmitted. High OC returns are generally caused by strong specular reflections from surfaces that are flat on scales much larger than the scale of the wavelength and are enhanced on slopes normal to the transmitted beam [*Campbell et al.*, 2009b]. However, if an incident beam reflects off a second surface such as a rock edge or other sharp terrain feature, it will change polarity for a second time and return to the same sense circular (SC) polarization as that which was transmitted.

As a surface becomes rough there is a higher likelihood a signal will exhibit double-bounce reflectance: on a "perfectly" rough surface, the amount of SC backscatter should equal the amount of OC backscatter, which will lead to a maximum CPR value of 1. However, values as high as 3 have been observed for lunar craters [*Campbell*, 2012; see *Carter et al.*, 2012]; values greater than 1 are also possible when observing water ice deposits, the result of coherent opposition backscatter effect within a low-loss media such as ice [see *Nozette et al.*, 2010; *Spudis et al.*, 2010; *Thompson et al.*, 2011; *Thomson et al.*, 2012; *Spudis et al.*, 2013].

This study uses radar data from the Miniature-Radio Frequency (Mini-RF) instrument on the Lunar Reconnaissance Orbiter (LRO) [e.g., *Nozette et al.*, 2010; *Raney et al.*, 2011; *Cahill et al.*, 2014] and ground-based radar from bistatic operations collected via the Arecibo and Green Bank observatories [*Campbell and Ward*, 2007] to determine the population of blocky material on the surface and subsurface on short length scales from CPR data. These data are then compared to roughness data on longer length scales obtained from laser altimetry using the Lunar Orbiter Laser Altimeter (LOLA), also on LRO [*Smith et al.*, 2010a]. Examining these data sets yields roughness measurements for a range of spatial and surficial length scales.

In order to examine the variation in roughness across these length scales, various geologic units were identified. Included in this study are volcanic domes of various ages, compositions, and emplacement styles, namely the Marius Hills, Rümker Hills, and Gruithuisen and Mairan domes; mare basalts from various provinces including Mare Imbrium, Mare Serenitatis, and Oceanus Procellarum; pyroclastic dark mantle deposits from Sinus Aestuum, Sulpicius Gallus, and Mare Vaporum; and two large, young impact craters, Copernicus and Tycho. The range of morphologies, ages, compositions, locations, and formation mechanisms should differentiate the units from each other. Likewise, the physical and compositional variations between the volcanic dome units may create distinct radar scattering and topographic roughness trends as well.
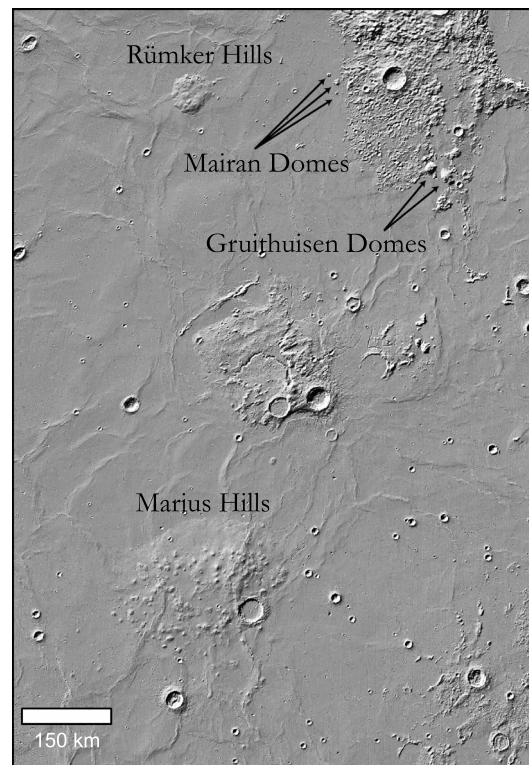
Figure 1. LOLA shaded relief image of the four volcanic dome units analyzed, located in Oceanus Procellarum: Marius Hills domes, Rümker Hills, Gruithuisen domes, and Mairan domes. The Marius Hills domes and the Rümker Hills are composed of mare-like basalt, although the Rümker Hills may be mantled with pyroclastic materials. The Gruithuisen and Mairan domes are composed of nonmare material similar to that of the highlands. Image centered on the Aristarchus Plateau, 309°E, 25°N.

2. Background

Four distinct volcanic dome units were analyzed for this study (Figure 1), which vary in both emplacement style and composition. The domes examined include the Marius Hills, Rümker Hills, and Gruithuisen and Mairan domes.

The Marius Hills complex contains the highest concentration of volcanic domes on the Moon. This region spans 35,000 km^2 [*Weitz and Head*, 1999], and the LOLA-derived relief across the plateau is 1 km [e.g., *Smith et al.*, 2010a]. Spectral analyses [*Sunshine et al.*, 1994; *Weitz and Head*, 1999] have shown that the Marius Hills had a complex geologic history, containing multiple mare units of distinct ages and composition. *Besse et al.* [2011] used spectra from the Moon Mineralogy Mapper (M^3), a NASA instrument payload aboard the Indian Space Research Organization's Chandrayaan-1 spacecraft, and determined the domes in the Marius Hills belong to a high-calcium pyroxene-bearing unit. These domes display similar spectra to the high-calcium pyroxene-rich maria regions characterized by *Besse et al.* [2011] and are highly likely to be composed of a similar mare basaltic unit. The recent analysis of this region by *Lawrence et al.* [2013] also concluded that the Marius Hills domes are of similar composition to the surrounding mare, although the range of volcanic morphologies, including the presence of volcanic cones, indicates that eruptive conditions were variable across the plateau.

Campbell et al. [2009b] analyzed the Marius Hills using S- and P-band (12.6 and 70 cm wavelength) ground-based radar. Results of this study found that P-band-derived CPR values of the domes were significantly higher (0.48–0.91) than in the surrounding mare (0.2–0.4) and suggested that the domes had enhanced near-surface rock abundances or rougher topography than typical mare lava flows (Figures 2a and 2b). In addition, *Lawrence et al.* [2013] also used Mini-RF data to correlate areas of enhanced radar backscatter in this region with surface block populations on lava flows and volcanic cones as determined from Lunar Reconnaissance Orbiter Camera (LROC) narrow angle camera (NAC) images.

The Rümker Hills (referred to as Mons Rümker by *Campbell et al.* [2009b]) is a volcanic complex with a diameter of 80 km containing over 30 coalesced domes in northern Oceanus Procellarum [*Weitz and Head*, 1999]. Clementine spectra of the region show that the domes are indistinguishable from the surrounding mare and are of similar composition to the Marius Hills domes [*Weitz and Head*, 1999]. However, the Rümker Hills complex lacks the clearly distinguishable lava flows and volcanic cones found in the Marius Hills region, potentially reflecting differences in eruption style between the two regions (Figure 2c). Additionally, *Campbell et al.* [2009b] observed the radar properties for Rümker are similar to those of the Aristarchus Plateau rather than the Marius Hills. Circular polarization ratio values for the Rümker Hills are generally lower than the surrounding mare, but also demonstrate lower echoes in P-band (70 cm) relative to S-band (12.6 cm) wavelengths. These low CPR values at both wavelengths suggest that there are few rocks larger than ~2 cm in diameter in the uppermost surface, as well as a paucity of decimeter-diameter and larger rocks in the upper 5–10 m of the Rümker Hills, leading *Campbell et al.* [2009b] conclude that the northern section of the Rümker Hills, if not the entire complex, is likely mantled by several meters of rock-poor material
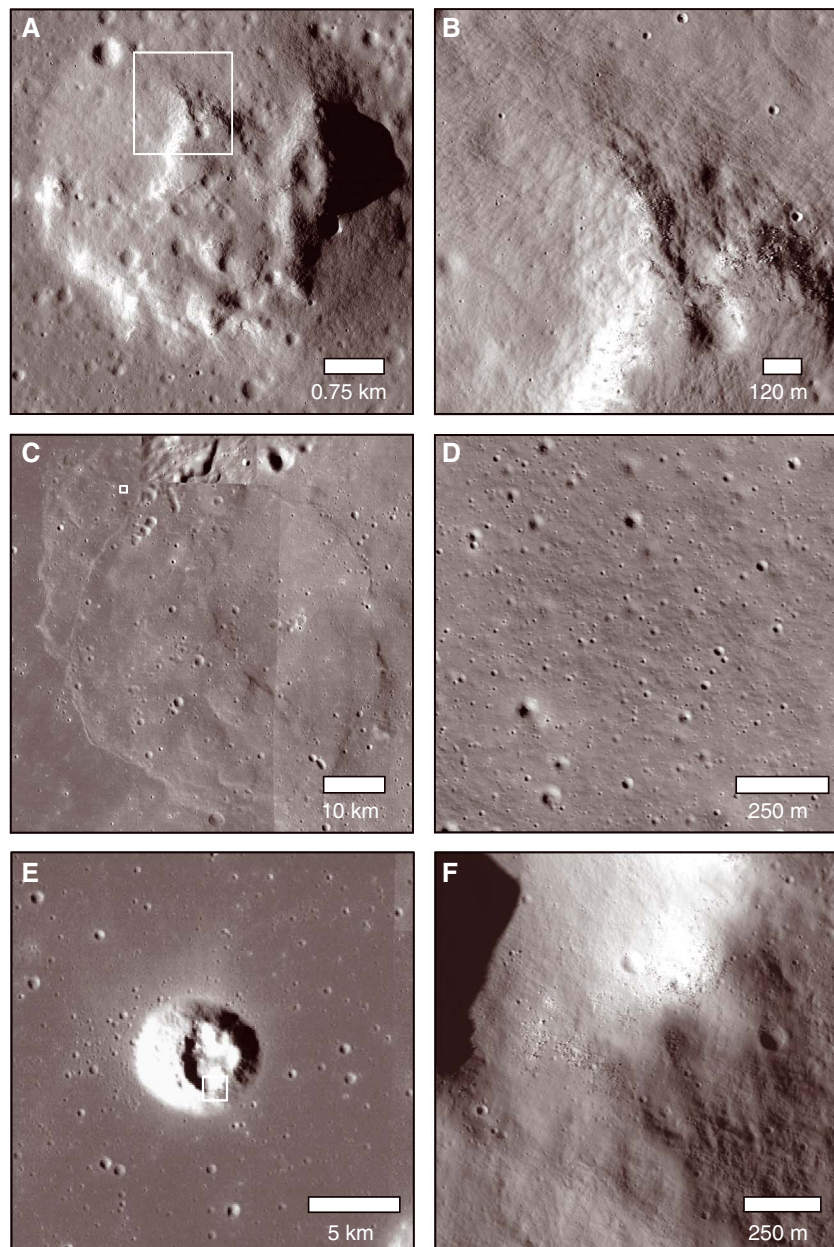
Figure 2. LROC images of various volcanic domes chosen for analysis. (a and b) Marius Hills dome, centered near 54.8°W, 14.2°N, LROC NAC image M102515241LE. (c) NW section of Rümker Hills, likely mantled by several meters of pyroclastic material, from *Campbell et al*. [2009b]. Image centered near 58.3°W, 40.7°N, global LROC wide angle camera (WAC) mosaic, and inset (d) LROC NAC image M107256767RE. (e) Mairan dome, centered near 48.4°W, 41.8°N, global LROC WAC mosaic, and inset (f) LROC NAC image M181495748RE. The domes vary widely in both surface texture and size. Note that these insets do not reflect the actual size of the analysis boxes used in this study but are used to illustrate variations in surface texture.

of possible pyroclastic origin (note smooth texture in Figure 2d). The similar composition of the Rümker Hills and Marius Hills, and apparently distinct emplacement mechanisms, provides an opportunity to differentiate roughness effects related to composition and emplacement style.

Two other volcanic dome units were included in this work, the Gruithuisen and Mairan domes (Figure 1). These large, steep-sided domes are morphologically and spectrally distinct from both the Marius Hills and the Rümker Hills domes, and are believed to have formed from silicic and/or viscous magma [*Weitz and Head*,

1999; *Wilson and Head*, 2003; *Glotch et al.*, 2010, 2011] (Figures 2e and 2f). Thermal emission spectra from the LRO Diviner lunar radiometer instrument show that at least some of these domes contain high-silica materials [*Greenhagen et al.*, 2010]. Terrestrial silicic lava domes have been studied using radar and are known to be extremely rough; *Plaut et al.'s* [2004] Airborne synthetic aperture radar-derived measurements of terrestrial silicic domes found CPR values of 0.3–0.95 at radar wavelengths of 5.6, 24, and 68 cm, with longer wavelengths yielding higher-CPR values. Most of the CPR variability in this data is due to changes in radar wavelength, although there is also a smaller variability due to incidence angle. As incidence angle increases from ~32° to ~50°, *Plaut et al.'s* [2004] results show a slight decrease in CPR (~0.1) for two silicic domes in the Inyo domes in California, while basaltic a'a and pahoehoe flows in Hawaii show moderate (0.1–0.2) increases in CPR over the same incidence angle range. Based on these radar data of volcanic domes from both the Marius Hills and terrestrial analog studies, it is reasonable to assume that both the Gruithuisen and Mairan domes will have higher CPR and enhanced surface roughness when compared to the surrounding mare basalts.

Three additional types of units were examined as a basis for comparison to the domes, including mare lava flows, dark mantle deposits, and impact craters. Mare lava flows include areas in Mare Imbrium, Oceanus Procellarum, Mare Serenitatis, and areas of the Marius Hills plains between domes. Dark mantle deposits include Sinus Aestuum, Sulpicius Gallus, and Mare Vaporum. Previous work has interpreted these regional dark mantle deposits as deposits of pyroclastic materials released during fire fountaining events in the early stages of large-scale basaltic volcanism [*Head*, 1974; *Weitz et al.*, 1998; *Gaddis et al.*, 2003]. Additional measurements have shown that pyroclastic deposits demonstrate low values of CPR (S-band CPR values of 0.18 in Sulpicius Gallus, and 0.08 in Mare Vaporum as recorded by *Carter et al.* [2009], for example), presumably caused by fine-grained volcanic ash mantling previously emplaced surfaces [*Gaddis et al.*, 1985; *Campbell et al.*, 2008; *Carter et al.*, 2009; *Saran et al.*, 2012]. Two young craters, Tycho and Copernicus, were also examined because of their notable roughness characterizations in previous studies [*Pettengill and Thompson*, 1968; *Zisk et al.*, 1974; *Bandfield et al.*, 2011; *Campbell*, 2012; *Carter et al.*, 2012]. Areas analyzed for each impact crater include the ejecta deposits (Figures 3a–3c) and crater interiors (Figures 3d–3f).

3. Methods

For each unit, near-surface roughness was assessed with two techniques, laser altimetry and radar, generating four data sets: RMS topographic planar offset (RMS TPO), median slope, S-band CPR, and P-band CPR, which are described in detail below. To ensure uniformity between these data sets, a standard box size of $0.2 \times 0.2°$ or ~6×6 km^2 was defined, and values reported here represent the average (median) of all data inside each box. A shaded relief map of the LOLA gridded elevation model with a resolution of 128 pixels/° provided a base map to identify the geologic features in the radar data. To assure coregistration of altimetry and radar measurements, the data sets were adjusted to match the LOLA base map using tie points based on a visual inspection of the data. The specific placement of each study box was chosen to encompass the maximum coverage of each geological feature, as well as to be positioned in an area covered by both LOLA and radar data, while excluding (to the fullest practical extent) surrounding surfaces and impact craters. In the case of the Marius Hills and Mairan domes, each box was roughly an adequate size to include the flank and summit of each dome. The Rümker Hills and Gruithuisen domes, however, are much larger than the $0.2 \times 0.2°$ box, and in these instances boxes were situated in various locations across each unit. In the case of Gruithuisen, boxes were drawn on both the flank and summit of both domes.

3.1. Altimetry

Every LOLA laser pulse samples the lunar surface in a five-beam X-shaped configuration, which allows sequential groups of spots to be grouped into longer profiles of the lunar surface [*Smith et al.*, 2010b]. The layout of the beams produces five parallel profiles of data that have a spacing of ~10–12 m, while each consecutive group of five spots is separated by ~57 m due to the velocity of the spacecraft and the laser pulse width of ~5 ns [*Smith et al.*, 2010b]. The altimeter has a single-shot timing precision of 0.7 ns, and a single pulse range precision of ~9 cm [*Smith et al.*, 2010a]. In order to calculate surface roughness, three consecutive groups of five spots were grouped together, for a total of 15 spots at full LOLA functionality. The longitude, latitude, and radius data from these spots were then used to generate a least squares best fit plane. To ensure robust least squares planes, a minimum of nine functioning spots was required over the three groups of spots
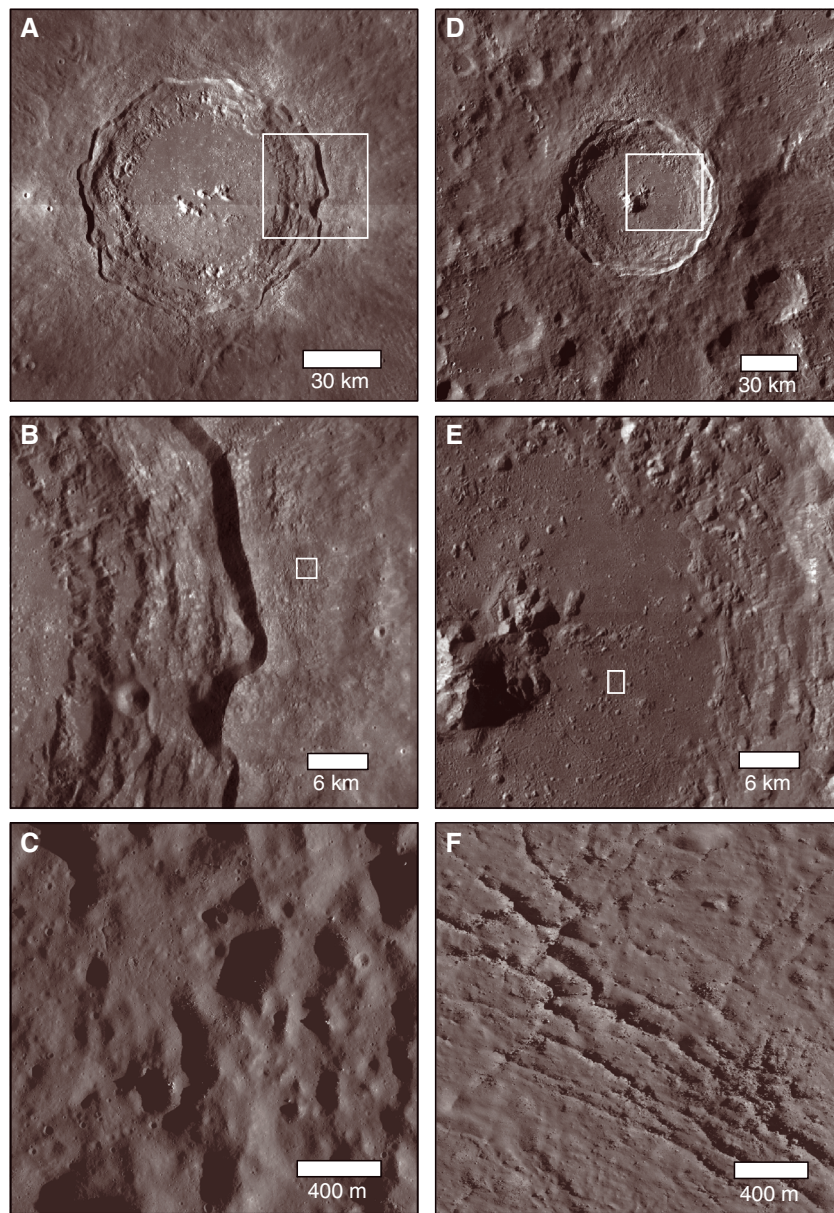
Figure 3. LROC images of the young craters chosen for analysis. (a) Copernicus crater, centered near 20°W, 9.5°N, and inset (b) on ejecta deposit, global LROC WAC mosaic. (c) Inset of ejecta deposit, LROC NAC image M177751830LE. (d) Tycho crater, centered near 11°W, 43°S, and (e) inset on crater floor, global LROC WAC mosaic. (f) Inset on floor of Tycho Crater, LROC image M129363095LE. The crater floor and ejecta deposit both exhibit extremely rough surface textures. Note that these insets do not reflect the actual size of the analysis boxes used in this study but are used to illustrate variations in surface texture.

Topographic roughness was then calculated by measuring the root-mean-square (RMS) offset of each altitude measurement from this idealized plane (similar to *Rosenburg et al.* [2011]) (Figure 4). This metric will be referred to as RMS topographic planar offset (RMS TPO). By this method, a perfectly smooth surface would yield a RMS TPO of zero, while larger RMS values correspondingly correlate to higher degrees of surface roughness. Due to the configuration of the beams and the velocity of the spacecraft, RMS TPO measures surface roughness on ~25 to 100 m length scales (25 m is the minimum spacing between LOLA laser spots and 100 m is based on the length of the plane used in the RMS calculation). The uncertainty in each LOLA altimetry measurement is ~9–12 cm in smooth terrain and increases in rough terrain [*Smith et al.*, 2010a]. Because the terrains analyzed in this study range from smooth to rough, the single-shot uncertainty was conservatively increased by a factor of 3 to 36 cm for all measurements. Assuming a Gaussian
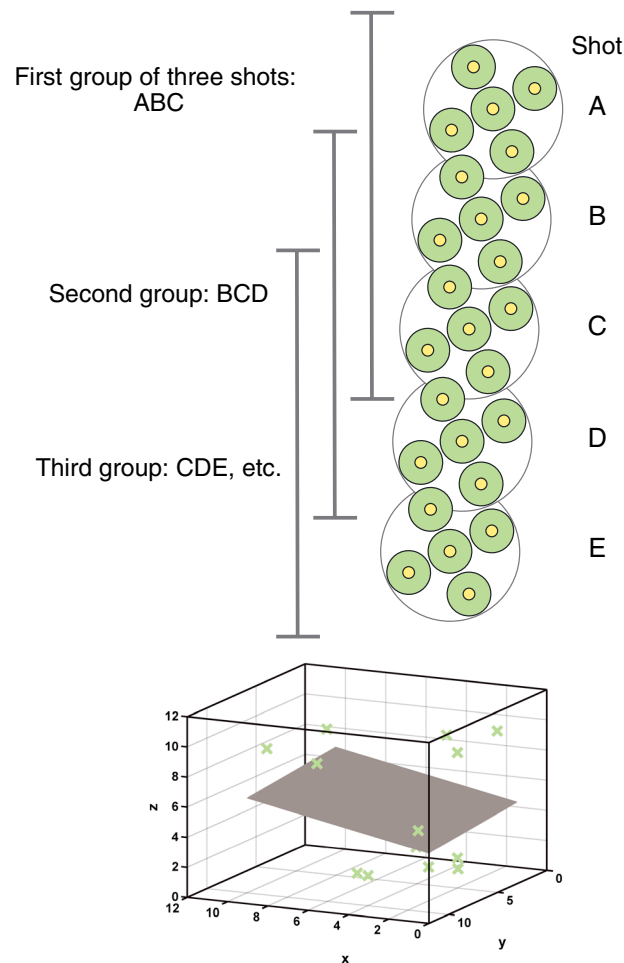
Figure 4. Schematic describing the methods used to calculate RMS topographic planar offset (RMS TPO) measurements. Three groups of LOLA spots are taken together (for example, shots A, B, and C), and these 15 data points are used to create a least squares best fit plane, from which the RMS offset is calculated at each data point. Note the yellow circles represent the footprint of each laser spot, and the green circles are the field of view of each detector, similar to Figure 1 in *Rosenburg et al.* [2011] and Figure 2 in *Smith et al.* [2010b]. The median slope is calculated on each plane from the angle between this plane and a horizontal plane. The next consecutive three groups of LOLA spots are then grouped (shots B, C, and D) to generate a new plane and new RMS TPO values. The topographic planar offset measurements in Table 1 are averages (medians) of the RMS offset values in each $0.2° \times 0.2°$ analysis box, and the median slope measurements are likewise averages (medians) of the local slopes within each box.

distribution of measurement errors, the two sigma uncertainty in the RMS TPO calculation is therefore 72 cm $(N\text{-}3)^{-0.5}$, where N is the number of points in the estimation (9–15) and N-3 is used because 3 degrees of freedom are used in calculating the best fit plane. This results in an estimated two sigma uncertainty in each RMS offset calculation of 20–30 cm. Each $0.2° \times 0.2°$ analysis box contains approximately 6000 LOLA points or ~400 least squares best fit planes. The individual RMS TPO measurements in each analysis box were averaged (by taking the median) to calculate the values and associated standard deviations observed in Table 1 and Figure 5.

The local slope of each feature over this baseline was also determined. Local slopes were calculated by measuring the angle between each best fit plane (generated from three groups of LOLA spots, as discussed above) and a horizontal plane (Figure 4). The local slopes within each $0.2° \times 0.2°$ analysis box were then averaged to calculate the median slope and standard deviation. We can determine an upper bound on the uncertainty in the median slope by assuming that the topography errors at one end of the measurement plane are two sigma (72 cm) in one direction from the true topography, and that the topography errors at the other end of the 100 m long measurement plane are two sigma in the other direction, for a total offset of the measurement plane of 1.4 m. The resulting two sigma uncertainty in the slope is arctan(1.4 m/100 m) = 0.8°. This is a strong upper bound because it assumes that topography errors occur in a highly correlated spatial pattern. In the more likely case, in which the RMS errors in topography are independent at each measurement point, the uncertainty in the median slope will be smaller, likely less than 0.4°.

Slope data are useful in distinguishing volcanic morphologies, so median slope values are listed in Table 1, and the correlations with other roughness measurements are listed in Tables 2 and 3.

Rosenburg et al. [2011] studied other aspects of short length scale roughness of the lunar surface between ~57 m and 2.7 km using LOLA altimetry, while *Kreslavsky et al.* [2013] used LOLA data to analyze roughness on somewhat longer length scales, namely baselines of 115 m to 1.8 km.

3.2. Radar

We utilized radar data in this study from both ground- and spacecraft-based observations. Planetary Data System (PDS)-released "Level 2" ground-based data at the P-band (70 cm wavelength) from the Arecibo

Table 1. Roughness Estimates for Each Geologic Feature, As Well As Associated Standard Deviation Values[a]

Feature	Central Longitude	Central Latitude	Topographic Planar Offset	Median Slope	S-Band CPR	P-Band CPR	P-Band Incidence
MH dome 1	301.36	11.71	0.95 ± 0.75	6.00 ± 7.11	0.52 ± 0.29	0.50 ± 0.21	67.81
MH dome 2	303.09	12.46	0.93 ± 0.80	3.83 ± 3.34	0.66 ± 0.37	0.35 ± 0.09	66.31
MH dome 3	304.52	13.09	1.04 ± 0.85	5.39 ± 4.04	0.58 ± 0.34	0.52 ± 0.18	65.08
MH dome 4	304.74	14.00	N/A	N/A	0.67 ± 0.37	0.83 ± 0.23	65.06
MH dome 5	305.51	12.16	0.98 ± 0.79	5.06 ± 5.39	N/A	0.55 ± 0.19	63.92
MH dome 6	305.66	11.61	0.98 ± 0.84	4.42 ± 3.31	0.67 ± 0.37	0.47 ± 0.13	63.66
MH dome 7	305.75	14.71	0.77 ± 0.63	5.78 ± 3.48	0.62 ± 0.35	0.55 ± 0.15	64.28
MH dome 8	306.21	11.80	0.77 ± 0.64	3.13 ± 3.17	0.51 ± 0.29	0.42 ± 0.11	63.17
MH dome 9	306.42	14.81	0.88 ± 0.86	6.85 ± 6.25	0.61 ± 0.34	0.48 ± 0.20	63.67
MH dome 10	307.63	11.79	0.68 ± 0.57	6.39 ± 4.86	0.73 ± 0.40	0.23 ± 0.05	61.82
Rümker 1	300.75	40.96	0.49 ± 0.57	1.96 ± 1.35	0.34 ± 0.19	0.31 ± 0.05	73.53
Rümker 2	302.19	40.31	N/A	N/A	0.48 ± 0.26	0.29 ± 0.09	72.27
Rümker 3	300.64	40.21	0.51 ± 0.30	2.46 ± 1.71	0.36 ± 0.20	0.17 ± 0.04	73.30
Gruith δ 1	320.05	36.29	0.72 ± 0.56	11.49 ± 4.94	0.56 ± 0.32	0.60 ± 0.16	60.93
Gruith δ 2	320.34	36.08	1.06 ± 0.87	8.03 ± 5.42	N/A	0.46 ± 0.12	60.61
Gruith γ 1	319.54	36.49	0.72 ± 0.40	12.85 ± 2.79	0.75 ± 0.39	0.56 ± 0.22	58.74
Gruith γ 2	319.21	36.56	0.85 ± 1.69	4.49 ± 4.55	0.55 ± 0.31	0.58 ± 0.18	61.64
Mairan top	311.60	41.79	1.12 ± 0.72	19.15 ± 7.80	0.52 ± 0.32	0.53 ± 0.17	66.83
Mairan middle	312.23	41.36	0.69 ± 0.38	8.71 ± 5.00	N/A	0.50 ± 0.19	66.20
Mairan bottom	312.30	40.80	0.63 ± 0.42	1.64 ± 3.38	N/A	0.35 ± 0.10	65.85
Oceanus 1	299.09	24.51	0.58 ± 0.40	0.98 ± 1.03	0.40 ± 0.21	0.34 ± 0.07	69.16
Oceanus 2	304.63	5.00	0.66 ± 0.60	1.36 ± 3.14	0.48 ± 0.26	0.23 ± 0.07	63.46
Oceanus 3	301.11	18.27	0.52 ± 0.57	0.84 ± 1.12	0.48 ± 0.24	0.35 ± 0.07	69.46
Imbrium 1	340.78	37.70	0.49 ± 0.35	0.88 ± 0.99	N/A	0.29 ± 0.09	48.93
Imbrium 2	335.19	35.92	0.71 ± 0.70	1.16 ± 1.82	0.45 ± 0.24	0.25 ± 0.05	49.60
Imbrium 3	331.64	36.72	0.52 ± 0.49	0.90 ± 0.87	0.46 ± 0.24	0.26 ± 0.06	53.89
MH plains 1	304.65	11.97	0.47 ± 0.28	1.12 ± 1.13	0.51 ± 0.27	0.33 ± 0.10	64.70
MH plains 2	307.33	12.55	0.57 ± 0.72	1.55 ± 2.72	0.47 ± 0.25	0.27 ± 0.08	62.27
MH plains 3	303.00	12.00	0.57 ± 0.55	1.29 ± 1.52	0.55 ± 0.29	0.29 ± 0.09	66.30
Serenitatis 1	25.63	15.76	0.47 ± 0.39	2.23 ± 1.81	0.40 ± 0.22	0.13 ± 0.03	31.91
Serenitatis 2	21.88	13.53	0.46 ± 0.50	1.72 ± 2.48	0.48 ± 0.25	0.11 ± 0.02	27.76
Serenitatis 3	27.79	12.86	0.44 ± 0.46	2.07 ± 4.48	0.52 ± 0.28	0.29 ± 0.15	31.66
Aestuum 1	345.36	6.54	0.76 ± 0.92	6.85 ± 5.38	0.56 ± 0.30	0.21 ± 0.04	24.91
Aestuum 2	350.72	6.67	0.52 ± 0.37	1.43 ± 1.24	0.52 ± 0.27	0.25 ± 0.06	20.45
Sulpicius 1	8.67	21.15	0.59 ± 0.25	5.41 ± 3.07	N/A	0.16 ± 0.04	28.45
Sulpicius 2	8.68	21.85	0.55 ± 0.33	8.21 ± 5.03	0.67 ± 0.36	0.19 ± 0.05	29.12
Sulpicius 3	7.51	21.72	0.62 ± 0.52	7.08 ± 3.70	0.51 ± 0.29	0.26 ± 0.14	28.80
Vaporum 1	5.21	11.19	0.54 ± 0.34	3.38 ± 2.54	0.50 ± 0.27	0.07 ± 0.01	24.48
Vaporum 2	7.21	12.27	0.48 ± 0.47	2.83 ± 2.15	0.43 ± 0.23	0.09 ± 0.02	18.14
Cop ejecta 1	337.85	9.30	1.07 ± 0.86	8.15 ± 3.92	0.75 ± 0.39	0.56 ± 0.18	32.82
Cop ejecta 2	342.01	10.85	0.75 ± 0.51	7.56 ± 4.00	0.80 ± 0.41	0.41 ± 0.14	29.98
Tycho ejecta 1	348.56	−41.45	1.68 ± 1.23	10.88 ± 5.88	N/A	1.29 ± 0.26	38.73
Tycho ejecta 2	349.84	−41.85	1.47 ± 1.00	6.09 ± 4.55	0.43 ± 0.24	1.26 ± 0.28	38.72
Cop floor 1	339.84	10.26	0.97 ± 0.78	2.21 ± 2.34	0.71 ± 0.37	0.65 ± 0.20	31.51
Cop floor 2	340.91	9.85	1.20 ± 0.81	11.75 ± 10.07	0.84 ± 0.43	0.78 ± 0.25	26.93
Tycho floor 1	349.45	−43.50	2.65 ± 1.16	4.97 ± 4.15	1.00 ± 0.48	1.54 ± 0.42	40.34
Tycho floor 2	349.60	−43.00	2.75 ± 1.82	6.73 ± 5.81	1.00 ± 0.48	1.43 ± 0.30	39.83
Tycho floor 3	349.23	−43.64	2.59 ± 1.98	3.91 ± 4.59	N/A	1.51 ± 0.21	40.52

[a]Roughness estimates represent the average (median) value of each 0.2° × 0.2° box. Longitude/Latitude are the coordinates about which the boxes were drawn. Units are as follows: Longitude/Latitude values are in degrees; Topographic planar offsets are in meters; Median slopes are in degrees; CPRs are dimensionless; P-Band incidence angles are in degrees. MH domes 1–10 are domes from the Marius Hills; Rümker 1–3 are areas on the Rümker Hills; and Gruith δ, γ, and Mairan top, middle, and bottom are the Gruithuisen and Mairan domes. Oceanus 1–3 and Imbrium 1–3 are mare units in Oceanus Procellarum and Mare Imbrium, while MH plains 1–3 are areas of mare between the domes in the Marius Hills. Serenitatis 1–3 are areas of Mare Serenitatis. Aestuum 1–2, Sulpicius 1–3, and Vaporum 1–2 are dark mantle deposits defined by *Weitz and Head* [1999]. Cop ejecta 1–2 and Tycho ejecta 1–2 are areas of the ejecta deposits around both craters, while Cop floor 1–2 and Tycho floor 1–3 are areas on the crater floors. N/A indicates no data in a particular parameter for a given feature. Context images for each measurement are provided in the supporting information.
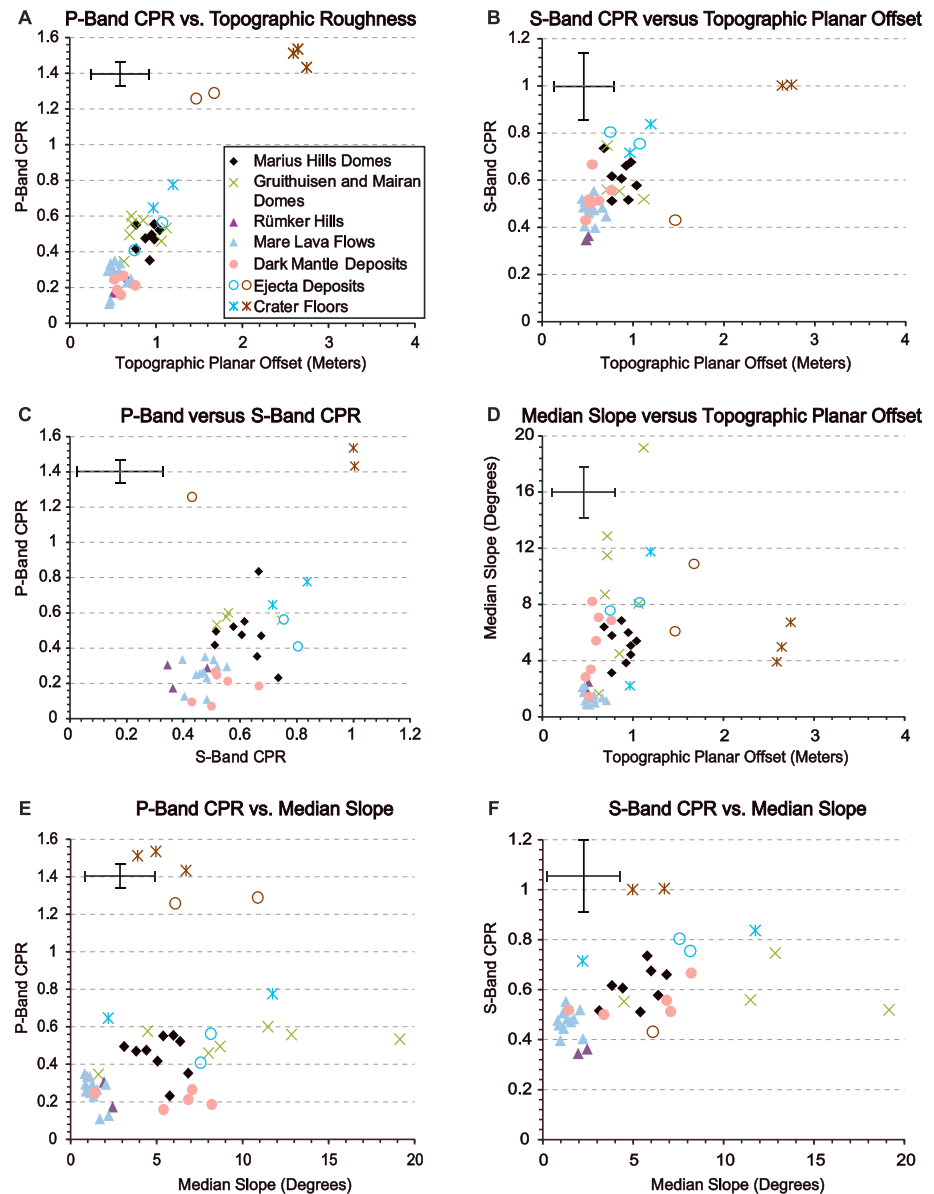
Figure 5. (a) P-Band CPR versus RMS topographic planar offset for the suite of geologic features. (b) S-band CPR versus topographic planar offset. (c) P-band versus S-band. (d) Median slope versus topographic planar offset. (e) P-band CPR versus median slope. (f) S-band CPR versus median slope. Crater features (ejecta deposits and crater floors) in blue refer to Copernicus crater, while crater features in brown refer to Tycho crater. It is important to keep in mind that these parameters measure roughness at different depths; RMS topographic planar offset measures roughness at the surface, while the CPR data measure surface and subsurface (volume scattering) roughness at depths dependent on the radar wavelength. Bars on each plot represent one-sigma ranges for each parameter, taken from Table 1. Note that these are a reflection of geologic variation rather than measurement uncertainties. A positive correlation is seen in all comparisons, to varying degrees. Correlation coefficients are in Tables 2 and 3. Parameters that are sensitive to roughness on the longest length scales correlate better than those which use length scales that are less similar.

and Green Bank Telescopes were used [*Campbell et al.*, 2007], sampled to a spatial resolution of 400 m/pixel. S-band (12.6 cm wavelength) data are measured by Mini-RF on LRO, with zoom capability to a spatial resolution of 15 × 30 m/pixel [*Nozette et al.*, 2010]. S-band CPR data from Mini-RF have an estimated relative uncertainty of ±0.1 [*Carter et al.*, 2012]. CPR data associated with Arecibo-based P-band radar have an uncertainty of <10% [*Campbell and Ward*, 2007].

Table 2. R^2 Values for the Comparisons of Roughness on Different Length Scales[a]

Parameter	Topographic Planar Offset	P-Band CPR	S-Band CPR	Median Slope
Topographic planar offset	–	–	–	–
P-band CPR	0.87	–	–	–
S-band CPR	0.53	0.43	–	–
Median slope	0.09	0.11	0.19	–

[a]R^2 values were generated from a linear trend line fit to the plots in Figure 5. For example, the R^2 value for the plot of RMS topographic planar offset against P-band CPR is 0.87. Note that RMS topographic planar offset has the longest baseline of the four parameters, ~25–100 m; P-band CPR is sensitive to rocks on decimeter-meter length scales up to a depth of 10 m; and S-band CPR is sensitive to rocks on centimeter-decimeter length scales up to a depth of 2 m. R^2 values for the parameters compared to median slope are also included, including the plot in Figure 5d.

Variations in CPR have been observed in conjunction with incidence angle, surface and near-surface roughness, and the dielectric properties of the target [see *Campbell et al.*, 2010; *Fa et al.*, 2011; *Thompson et al.*, 2011; *Carter et al.*, 2012]. Earth-based Arecibo data can range in incidence angle from <20° to 90° at the limbs in P-band nearside radar [*Fa and Wieczorek*, 2012]. We discuss the sensitivity of the P-band CPR observations to incidence angle in section 4.1.4.

The Mini-RF spacecraft maintains a fixed nominal incidence angle of 45°, preventing large variations in incidence angle (which for flat surfaces can range up to 48–55°) [*Raney et al.*, 2011; *Carter et al.*, 2012]. However, slight variations may exist between orbits which could contribute to CPR variation, although these variations are expected to be small.

Certain Mini-RF strips have been observed to contain range-direction gradients which can skew CPR data to higher values by up to ~0.2–0.3 [*Carter et al.*, 2014]. To compensate for this effect, any analysis regions which were located in areas of artificial enhancement due to gradient effects were removed from this study.

Along with sensitivity to surface roughness, radar is also sensitive to volume scattering in the subsurface to a depth of ~10–20 wavelengths, depending on the composition of the material (titanium, which is present in varying degrees in mare basalts in the mineral ilmenite, is strongly attenuating and limits probing depth and in turn, volume scattering) [*Campbell et al.*, 2008]. Using this relationship, S-band (12.6 cm wavelength) radar can penetrate the surface up to 1–2 m in typical mare regolith [*Campbell et al.*, 2009b]. Additionally, this wavelength is sensitive to surface and suspended rocks ~2 cm and larger in diameter. Likewise, P-band (70 cm wavelength) radar can achieve a depth about 5 times deeper (~5–10 m, depending on composition) and can detect rocks ~10 cm and larger [*Campbell et al.*, 2009b]. The S-band CPR data are therefore sensitive to surface and subsurface roughness on centimeter-decimeter length scales (up to 1–2 m), while P-band CPR is sensitive to roughness on decimeter-meter scales (up to 5–10 m). Because high titanium concentrations are known to diminish returning radar echoes (*Campbell et al.* [2009a] noted a marked decrease in CPR values in regions of >6 wt % TiO_2), an analysis was performed of TiO_2 abundances across the measurement sites using a 2° × 2° titanium map of Lunar Prospector data [*Prettyman et al.*, 2006]. From this analysis, it is apparent there is not a correlation between titanium content and CPR values at the locations studied in this work.

Table 3. R^2 Values for the Comparisons of Roughness on Different Length Scales (Tycho Omitted)[a]

Parameter	Topographic Planar Offset	P-Band CPR	S-Band CPR	Median Slope
Topographic planar offset	–	–	–	–
P-band CPR	0.61	–	–	–
S-band CPR	0.39	0.35	–	–
Median slope	0.36	0.28	0.27	–

[a]R^2 values were generated from a linear trend line fit to the plots in Figure 5, with data points from Tycho crater omitted as possible outliers. All other comments from the footnote to Table 2 also apply here.

4. Results

4.1. Measurements of Individual Units

For each $0.2° \times 0.2°$ analysis box, the median values of the topographic roughness, P-band and S-band CPRs, and local slope are reported in Table 1, as well as standard deviation values for each parameter. The standard deviation values shown in Table 1 are all significantly larger than the measurement errors associated with these quantities. Thus, the uncertainties listed in Table 1 represent the actual geologic variability of these quantities in each study region.

The data sets for each measured parameter were compared against each other (Figure 5) to determine the relationship between roughnesses on different length scales on the surface and subsurface. The following is a description of characteristic signatures exhibited by each unit.

4.1.1. Smooth and Rough Terrains: Dark Mantle Deposits, Maria, and Crater Features

Consistent with expectations, the dark mantle deposits and maria had the lowest roughness signatures, although the dark mantle deposits were indistinguishable from the mare units in all of the roughness parameters we defined. Likewise, both the crater floor and ejecta deposit units exhibit the highest roughness values in every parameter (Figures 5a–5d). However, there exists significant variability within each geologic unit; for example, two ejecta deposit regions demonstrate anomalously low values of P-band CPR and RMS topographic planar offset (Figure 5a), which is not reflected in the S-band CPR data. Additionally, the volcanic domes, maria, and dark mantle deposits follow a distinct trend line from impact-generated terrains (Figures 5b and 5d especially). This is attributable to the distinct physical processes that formed these different units.

Measurements of terrestrial volcanic units yield RMS height values as low as 0.55–7.94 cm for Kilauea basalts over a 1 m baseline and 5.8–52.4 cm over a 10 m baseline [*Campbell and Shepard*, 1996; *Shepard et al.*, 2001]. The RMS topographic planar offset values of lunar mare surfaces, 44–71 cm over a 25–100 m baseline (Table 1), are somewhat larger than those observed at Kilauea. This is expected, as longer measurement baselines will yield higher-RMS heights [*Shepard et al.*, 2001]. Using a scaling factor of approximately the square root of the length factor, assuming a value of the Hurst exponent of $H = 0.5$, the RMS height should effectively double from a 10 m to ~50 m baseline, as $\sqrt{5}$ ~2.2. This is consistent with the observed increase in RMS height across the data sets.

Conversely, blocky, andesitic flows have RMS height variations of up to 165 cm on a 10 m baseline [*Shepard et al.*, 2001]. The terrestrial andesitic flows are rougher than the lunar mare even at the shorter 10 m baseline, supporting the concept that lunar basalts form similar surface roughnesses to those of terrestrial basalts. Mare lava flows characteristically have very small surface slopes (Figure 5d), which have been inferred to reflect formation by lava with low viscosity or high effusion rates [*Wilson and Head*, 1981] which fills in local topographic lows in the preexisting surface. This agrees with terrestrial measurements of lava flows, which show very low local slopes (<0.2°) [*Gaddis et al.*, 1990]. While the lunar mare slopes are higher (<3°, Table 1) than the local slopes of terrestrial basalt flows, the mare flows nevertheless have the lowest median slopes observed in our data set (Figure 5d).

On the other hand, the dark mantle deposits typically have much larger local slopes (Figure 5d). The dark mantle deposits are thought to have formed as pyroclastic deposits, which would drape over the preexisting topography without necessarily smoothing out existing slopes [*Head*, 1974]. Not surprisingly, crater floor deposits and ejecta deposits typically have large local slopes (Figure 5d).

4.1.2. The Marius Hills, Gruithuisen, and Mairan Domes

The various dome units generally fall between the smooth and rough geologic features in roughness. There is a large total range in P-band CPR for the Marius Hills, 0.23–0.83, although most are tightly clustered in the range ~0.4–0.6 (Figure 5c), while values for topographic planar offset and S-band CPR are both tightly clustered (Figure 5b). The S-band CPR values for the 10 selected Marius Hills domes measured by Mini-RF are 0.44–0.64 (Table 1 and Figure 5b). *Campbell et al.* [2009b] reported S-band CPR for the Marius Hills measured using the Arecibo and Green Bank radio telescopes. Although they measured CPRs of up to 1.2 in very localized regions, the bulk of their dome measurements appear to be consistent with our results, particularly considering the difference in resolution between the two studies (500 m per pixel in Campbell's study versus an averaging box of 6×6 km in our study). The Gruithuisen and Marian domes, however, exhibit a small spread in P-band CPR, S-band CPR, and RMS topographic planar offset (Figures 5a and 5b). The slopes of the
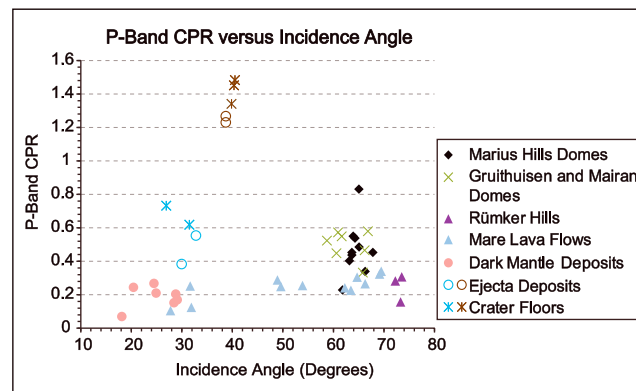
Figure 6. P-band CPR as a function of incidence angle. Although there is some dependence of CPR on incidence angle, the CPR variability is primarily due to differences in geologic setting. Crater feature symbols (ejecta deposits and crater floors) in blue refer to Copernicus crater, and those in brown refer to Tycho crater.

Gruithuisen and Mairan domes are larger than those for the Marius Hills domes, between ~2 and 19° (Table 1). These slopes, while larger than those of the less silicic lunar domes, are smaller than terrestrial values of slopes for the silicic Inyo Domes [*Plaut et al.*, 2004]. *Plaut et al.'s* [2004] terrestrial calculations of RMS height for these domes are fairly similar albeit on a shorter length scale, with a mean value of 62 cm at a 20 m profile length, compared to the lunar RMS topographic planar offset values of ~63–112 cm on a 25–100 m length scale (Table 1).

The Marius Hills and the Gruithuisen and Mairan domes have different compositions: the Marius Hills are basaltic, while the Gruithuisen and Marian domes are more feldspathic [*Sunshine et al.*, 1994; *Weitz and Head*, 1999; *Wilson and Head*, 2003; *Campbell et al.*, 2009b; *Besse et al.*, 2011; *Glotch et al.*, 2010, 2011; *Lawrence et al.*, 2013]. Lava flow morphology depends on lava viscosity and thus in part on composition, leading to the hypothesis that there could be a discernible difference in roughness measurements between these compositional groups. However, we find no significant distinction in surface roughness values between the Marius Hills and the Gruithuisen and Mairan domes across the CPR and RMS planar offset data sets. Gravity evidence reveals the presence of a large magma chamber system beneath the Marius Hills [*Kiefer*, 2013]. One possibility is that magma which partly solidified in this magma chamber later erupted as a partially crystalline mush, forming the various Marius Hills domes. These crystals would increase the viscosity of the erupting magma relative to the viscosity of liquid basalt. This more viscous magma might contribute to the short length scale roughness observed in the Marius Hills and thus minimizes the observed differences between the Marius Hills and the Gruithuisen and Mairan domes. This proposed geologic history of the Marius Hills mirrors the conclusions of *Heather et al.* [2003], *Campbell et al.* [2009b], and *Lawrence et al.* [2013]. On the other hand, our measurements of local slope show a strong difference between the various volcanic fields, with the Gruithuisen and Mairan domes demonstrating the largest median slopes measured in this study (Figure 5d). These high slopes are likely a manifestation of the high magma viscosity at the time of eruption [*Wilson and Head*, 2003]. An alternative explanation for the similarity of these groups of domes in this parameter space is that postemplacement modification, such as regolith formation, has masked any original differences in surface roughness.

4.1.3. Rümker Hills
Unlike the other three dome units, the Rümker Hills do not plot between the smooth and rough end-member geologic features. In P-band CPR, S-band CPR and RMS planar offset, the roughness signatures appear extremely low (Figures 5a and 5b). In all cases, the Rümker Hills are indistinguishable from the mare lava flows and dark mantle deposits. This supports the theory that the Rümker Hills may be mantled by multiple meters of fine-grained pyroclastic material [*Weitz and Head*, 1999; *Campbell et al.*, 2009b].

4.1.4. Effects of Incidence Angle
As noted earlier, the P-band CPR observations were made for incidence angles ranging from 18° to 73°, and incidence angle is known to have an effect on CPR values. However, the Level 2 data released to the PDS have been normalized to reduce the effect of incidence angle on echo brightness [*Campbell and Ward*, 2007]. Figure 6 plots the P-band CPR values as a function of incidence angle. Mare lava flows have been measured for incidence angles between ~27 and 70°, with P-band CPR increasing from 0.10 to 0.34 over that range. The dark mantle deposits do not show a distinct trend in CPR with incidence angle, although incidence angles for these measurements only range from 18 to 30°. The various volcanic domes are all measured at high incidence angle, but taken as a group, they do not show a correlation with incidence angle. As noted earlier, the CPR for the volcanic domes does depend on geologic setting, with the Rümker Hills having

a notably lower CPR than the other domes. The crater floor and ejecta deposit CPRs also depend primarily on geologic setting, with the Tycho CPR values being systematically much larger than the Copernicus CPR, possibly a result of Tycho's younger age.

Plaut et al. [2004] observed modest changes (0.1–0.2) in CPR at terrestrial silicic domes and basaltic lava flows at incidence angles between 30° and 50° for wavelengths of 5.6, 24, and 68 cm. At 24 and 68 cm, the geologic setting (silicic or basaltic) had a far stronger effect on the CPR than the incidence angle, with CPR differences of up to 0.5 between silicic and basaltic surfaces at P-band (68 cm). *Thompson et al.'s* [2011] radar scattering model for the average lunar surface shows only a small change (0.08) in CPR between incidence angles of 30° and 70° at S-band (13 cm wavelength). The change in CPR with incidence angle is even smaller for rough lunar surfaces, which is consistent with the amplitude of changes in CPR with angle observed by *Plaut et al.* [2004] for rough silicic domes and smoother basaltic flows. *Fa and Cai* [2013] found that changes in the incidence angle of 30° along the walls of small, bowl-shaped lunar craters change the S-band CPR by 0.1–0.2. All of these results confirm that the large variation in P-band CPR seen in our study (0.07–1.48) must be dominated by geologic setting, with the effect of variable incidence angle being of secondary importance.

4.2. Comparison of Roughness Measurements

Figure 5 shows that there is a positive correlation among the various measurements of roughness that are explored in this paper. The strength of this correlation can be assessed by performing a linear regression analysis. Table 2 shows the linear correlation coefficients (R^2) for the various pairs of data sets. Figures 5a–5c show strong correlations among the RMS TPO, P-band CPR, and S-band CPR. This is confirmed in Table 2, where the correlations (R^2) are between 0.43 and 0.87. Student's t tests show these correlations are all statistically significant at more than 99% confidence. On the other hand, all of the correlations involving median slope are small (0.09–0.16) and are not statistically significant. Figures 5d–5f show that no other shape correlation function would be a good fit to the median slope versus RMS TPO data.

Examination of Figure 5 suggests that some of the data points related to Tycho crater (brown symbols) might be outliers that may disproportionately affect the correlation line among the data points. This is particularly obvious in Figures 5b, 5d, and 5e. We have tested the possible influence of the Tycho data points on the correlation lines by removing all Tycho data points from the analysis and recalculating the least squares best fit lines among the various model parameters, with results shown in Table 3. Omitting the Tycho points has the effect of reducing the larger correlation coefficients. For example, the TPO versus P-band CPR correlation coefficient is reduced from 0.87 (all data) to 0.61 (Tycho omitted), but a t test confirms that this is still statistically significant at the 99% confidence level. With Tycho omitted, TPO versus S-band CPR is now significant at the 98% confidence level and S-band CPR versus P-band CPR is significant at the 95% confidence level. Interestingly, the correlations between slope and the other study parameters are substantially stronger when Tycho is omitted, with the TPO versus median slope correlation being significant at the 98% confidence level. The high levels of statistical confidence in these four correlations suggest that they are quite likely to be real. The correlations between S-band CPR and slope and between P-band CPR and slope are significant at the 90% level when Tycho is omitted. Although these two correlations between slope and CPR may also be real, we will not discuss them further in this paper.

The observation that Tycho appears to be an outlier in all of the data sets may be due its young age (109 Ma, [*Drozd et al.*, 1977]). Unlike all of the other structures considered in this study, Tycho has not had time to develop a meaningful thickness of regolith to mantle the surface. Tycho's regolith thickness would be just 11 cm assuming the regolith accumulation rate of *Quaide and Oberbeck* [1975]. Thus, the age of a feature is probably one of the important parameters in controlling the topographic roughness and radar CPR signatures. In the remaining part of this discussion, we will use the correlations from Table 3 in which Tycho is omitted from the calculations. The strongest relationship between the various measurements is between P-band CPR and RMS topographic planar offset (Figure 5a), with an R^2 value of 0.61 (Table 2). This is likely due to the similar sensitivity of the two parameters; P-band wavelength radar is sensitive to rocks ~10 cm and larger [*Campbell et al.*, 2009b], including large, meter-scale blocks and boulders present on the surface, as well as those buried to a depth of ~5–10 m. Surficial roughness variations at the scale of multiple meters can contribute directly to RMS TPO. In addition, large rocks and boulders are known to be preferentially found on topographically rough terrains on the Moon [e.g., *Bandfield et al.*, 2011], where regolith development has not yet mantled the surface.

The correlation between S-band CPR and RMS TPO (Figure 5b) is weaker than that of P-band CPR with RMS TPO, but is still statistically significant at the 98% confidence level. This weaker signature is likely due to a shorter (12.6 cm) wavelength and hence sensitivity to roughness at a shorter length scale than for P-band and TPO observations. Likewise, the shorter wavelength of S-band data limits the probing depth to ~1 m, while P-band data can penetrate the surface to a depth of ~5–10 m in typical regolith. Moreover, the smaller rocks sensed by S-band CPR may be more easily masked by regolith development (i.e., comminution and burial) over time.

The correlation between P-band and S-band CPRs is not as strong as the correlation of either CPR value with RMS TPO but is nevertheless significant at the 95% confidence level. This is due to several factors including the sensitivity to different materials and depths, the difference in incidence angles between the observations, and the influence of TiO_2 and FeO on both data sets. Therefore, the presence of such a correlation between P- and S-band CPRs suggests that the concentration of meter-scale rocks on the surface and at depth are partially but imperfectly correlated with the concentration of centimeter-scale rocks at shallower depths.

The correlations among the data sets shown in Table 3 may seem surprising for two reasons. First, the LOLA altimeter TPO results probe roughness on length scales of 25 to 100 m, while the P-band CPR probes roughness at 5–10 m scales and the S-band CPR probes roughness at 1–2 m scales. However, topographic roughness at short length scales is known to exhibit fractal behavior [*Campbell and Shepard*, 1996; *Shepard et al.*, 2001; *Rosenburg et al.*, 2011]. Thus, regions of the Moon with high TPO roughness at 25–100 m length scales are also likely to be rougher than average at length scales of a few meters, although the amplitude of the roughness does not need to be the same at the various length scales.

A second possible surprise in these results is related to the radar scattering mechanism. High CPR values imply that a large fraction of the radar beam has experienced multiple radar reflections. Although it is possible to achieve multiple reflections solely with surface topography as the scattering surface, volume-scattering off buried rock surfaces can enhance the likelihood of achieving the necessary double-bounce reflection geometry. On the Moon, the dry regolith reduces radar absorption relative to moist terrestrial soil and may enhance volume scattering relative to Earth [*Campbell et al.*, 2009b]. Additionally, scattering off of rough, buried lava flows appears necessary to explain some high CPR mare regions [*Campbell et al.*, 2009a; *Campbell*, 2012]. However, our results show that there is a very strong relationship between surface roughness and radar CPR, particularly at the P-band (Table 2).

A possible explanation is that topographic roughness and volumetric roughness in the uppermost regolith are spatially correlated. Figure 7 illustrates one scenario for how topographic roughness evolves locally with time on the Moon. Various geologic processes can expose a rock on the lunar surface (Figure 7a). As time progresses, repeated impacts and thermal processes will work to fracture the rock and partially bury it (Figure 7b). Eventually, ballistic sedimentation of impact ejecta will drape material over the rock, burying it while preserving a muted topographic surface expression of the original object (Figure 7c). Although the topographic expression will be increasingly muted with greater depth, burial to several rock diameters or more may be required to fully destroy the associated topographic signature.

Recent work by *Basilevsky* [2013] has shown that meter-scale rocks will be 99% destroyed in 150–300 Ma. Simple calculations show that with a regolith accumulation rate of 1 mm/Ma [*Quaide and Oberbeck*, 1975], a rock 2 m in diameter will be destroyed and the fragments will be buried by regolith in 750 and 1200 Ma (destruction is defined as the point when the largest rock fragment is <0.5 the original rock mass, as defined by *Gault and Wedekind* [1969]) for a destruction rate of 150 and 300 Ma, respectively [*Basilevsky et al.*, 2013]. Moreover, the remaining fragments would measure ~60 cm in diameter, which would be detectable by P-band radar. This could explain the correlation between surface roughness measured by TPO and surface/volume scattering measured by the P-band radar.

A similar style of evolution with time would be expected for other forms of surface topographic roughness, such as a'a lava flows. This process would cause a correlation between surface roughness and buried volume-scattering elements and could contribute to the correlation between RMS TPO roughness and radar CPR observed in this study. This roughness evolution is distinct from one that would be observed in fluvial environments on Earth, where gradual deposition of fine-scale sediment might eventually bury rocks, leaving little or no topographic expression.
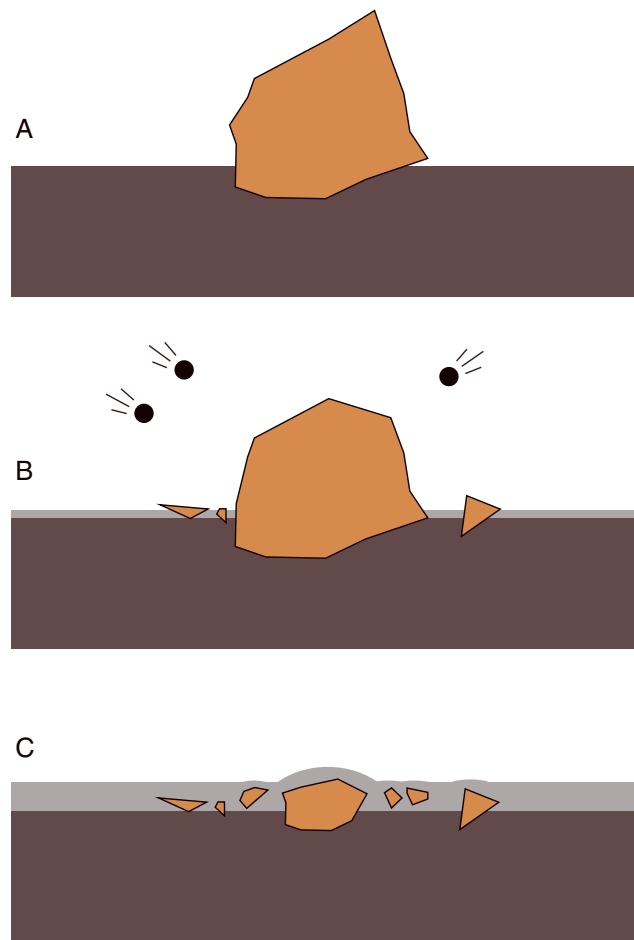
Figure 7. Schematic evolution of surface roughness with time. (a) A rock initially exposed on the lunar surface. (b) Repeated impacts from small-scale impacts fracture the rock, and fragments are buried by accumulating regolith. (c) Subsequent burial of the rock by impact-emplaced ejecta tends to drape material over the rock, so that some surface relief remains apparent even after the rock is completely buried.

5. Discussion

The domes which are composed of a more basaltic composition, namely the Marius Hills and the Rümker Hills, were expected to demonstrate different roughness signatures in this parameter space to the Gruithuisen and Mairan domes, which are relatively more silicic. This was not observed, however, as the Marius Hills, Gruithuisen, and Mairan domes appear comparably rough in all four parameters. The lack of clear distinction between the compositional groups may be explained by one of two hypotheses. First, lunar basaltic magmas may be capable of forming comparably rough surfaces as silicic magmas (which is broadly similar to the conclusions by *Campbell et al.* [2009b]), in which case the compositional distinction presented earlier is irrelevant.

A second hypothesis is that both sets of domes were emplaced with distinct roughness characteristics, but erosion and accumulation of regolith on the domes sufficiently smoothed their surfaces so as to make them appear comparably rough in this parameter space. Surface rock abundance decreases as age after emplacement increases [see *Bandfield et al.*, 2011]; a surface is reworked and smoothed over time, making surface roughness vary as a function of age. This process does not occur rapidly, as large rocks have a longer survival time than small rocks [*Hörz et al.*, 1975]. It is unclear how much age difference, if any, exists between the Marius Hills and the Gruithuisen and Mairan domes. The Marius Hills are mapped as Upper Imbrian (3.2–3.8 Ga) by *Wilhelms* [1987] and as Hermann Formation and older (3.0–3.6 Ga) by *Whitford-Stark and Head* [1980]. On the other hand, *Huang et al.* [2011] proposed a much younger cratering age of 1–1.5 Ga for the Marius Hills. The Gruithuisen and Mairan domes, meanwhile, were found to have ages between 3.3 and 3.6 Ga by *Head and McCord* [1978], and more recently the Gruithuisen domes were dated to the early part of the Late Imbrian (3.72–3.85 Ga) by *Wagner et al.* [2002]. The Gruithuisen and Mairan domes therefore may have been much rougher just after their emplacement, yet development of regolith may have eroded them to a similar roughness of the (possibly) younger Marius Hills domes.

The fourth dome unit, the Rümker Hills, was also distinct from the other dome units, plotting closer to the pyroclastic deposits and mare lava flows. The theory that the Rümker Hills are mantled by several meters of pyroclastic material is supported by these data, although the material which formed the Rümker Hills and is underlying the pyroclastic material is still unknown. However, the Rümker Hills yield very low P-band CPR values. Due to the probing depth of 70 cm wavelength radar, at least 5–10 m of fine-grained rock-poor material is necessary to create such low signatures.

Previous work has found a transition in surface roughness of length scales around 1 km, which is reflected in values of the Hurst exponent [*Rosenburg et al.*, 2011]. *Kreslavsky et al.* [2013] also found a poor correlation

between roughness on hectometer scales and kilometer scales, which agrees with the results from *Rosenburg et al.* [2011]. This distinction in roughness signatures is due to disparate surface processes occurring on each length scale; roughness on shorter (hectometer) length scales is dominated by regolith accretion and recent meteoritic impacts, while longer (kilometer) length scale roughness reflects large-scale surface modifications such as impactors or volcanism from the early stages of lunar geologic history [*Kreslavsky et al.*, 2013].

These large-scale processes may be analogous to those which are controlling surface roughness on smaller scales as well. Meter-scale rocks and boulders are exposed to the surface through a relatively small number of ways, including impact events, volcanism, and mass-wasting off steep slopes. Conversely, small-scale erosion from micrometeorite bombardment and impact gardening occurs constantly across the lunar surface. Due to this difference in modification rate and style, it is reasonable to assume that the factors controlling surface modification and burial on the smallest scales are independent from those that are controlling larger-scale alterations. This helps to explain why there is a stronger correlation between parameters which measure roughness on the longest length scales (Table 2).

The roughest surfaces measured in this study are on the crater floor and ejecta deposit of the young impact crater Tycho, whereas the floor and ejecta deposit of Copernicus crater are similar in roughness to many of the volcanic domes. Based on crater density, Tycho is the youngest large crater on the lunar near side [*Wilhelms*, 1987], with a likely radiometric age of about 109 million years [*Drozd et al.*, 1977]. Although Copernicus is also young compared to most lunar features, its superposed crater density is about an order of magnitude larger than Tycho [*Wilhelms*, 1987] and it has a possible radiometric age of around 800 million years [*Barra et al.*, 2006]. A plausible interpretation of the measured surface roughness for the two craters is that the Tycho results represent near-pristine roughness, whereas the short length scale roughness of Copernicus has begun to be reduced by regolith formation. However, with a sample of just two craters, it is difficult to test alternative models for roughness evolution with time.

6. Conclusion

Using the RMS topographic planar offset measurement from LOLA, as well as P- and S-band radar CPR measurements, the surface roughness at various length scales for lunar volcanic features was assessed. These three measures of roughness are all correlated at greater than 99% statistical confidence. The strongest relationship observed is between P-band CPR and RMS topographic planar offset. However, the strength of these relationships weakens as the length scale sensitivities of the parameters become less similar. This is likely due to distinct processes which are controlling surface modification; roughness on longer length scales, detectable by RMS planar offset and P-band CPR, is dominated by surface and subsurface rocks and boulders, which are emplaced due to large events such as large impacts, volcanism, or mass wasting. S-band CPR, while also sensitive to these large-scale events, is also sensitive to small-scale roughness such as erosional regolith processes.

In addition, the Marius Hills appear indistinguishable from the Gruithuisen and Mairan domes in the roughness data, despite their variations in composition. Conversely, the Rümker Hills are distinct from the other dome units and have roughness signatures more similar to smoother mare and dark mantle deposit units.

References

Bandfield, J. L., R. R. Ghent, A. R. Vasavada, D. A. Paige, S. J. Lawrence, and M. S. Robinson (2011), Lunar surface rock abundance and regolith fines temperatures derived from LRO Diviner Radiometer data, *J. Geophys. Res.*, 116, E00H02, doi:10.1029/2011JE003866.

Barra, F., T. D. Swindle, R. L. Korotev, B. L. Jolliff, R. A. Ziegler, and E. Olson (2006), ^{40}Ar/^{39}Ar dating of Apollo 12 regolith: Implications for the age of Copernicus and the source of nonmare material, *Geochim. Cosmochim. Acta*, 70, 6016–6031.

Basilevsky, A. T. (2013), Survival times of meter-sized boulders on the surface of the Moon, *Planet. Space Sci.*, 89, 118–126, doi:10.1016/j.pss.2013.07.011.

Besse, S., J. M. Sunshine, M. I. Staid, N. E. Petro, J. W. Boardman, R. O. Green, J. W. Head, J. F. Isaacson, J. F. Mustard, and C. M. Pieters (2011), Compositional variability of the Marius Hills volcanic complex from the Moon Mineralogy Mapper (M^3), *J. Geophys. Res.*, 116, E00G13, doi:10.1029/2010JE003725.

Cahill, J. T. S., B. J. Thomson, G. W. Patterson, D. B. J. Bussey, C. D. Neish, N. R. Lopez, F. S. Turner, R. K. Raney, and P. D. Spudis (2014), The miniature radio frequency instrument's (Mini-RF) global observations of Earth's Moon, *Icarus*, doi:10.1016/j.icarus.2014.1007.1018.

Campbell, B. A. (2012), High circular polarization ratios in radar scattering from geologic targets, *J. Geophys. Res.*, 11, E06008, doi:10.1029/2012JE004061.

Campbell, B. A., and M. K. Shepard (1996), Lava flow surface roughness and depolarized radar scattering, *J. Geophys. Res.*, 101(E8), 18,941–18,951, doi:10.1029/95JE01804.

Campbell, B. A., and J. Ward (2007), Dual-polarization calibrated radar map of the Moon, ARCB/NRAO-L-RTLS/GBT-4/5-70CM-V1.0, NASA Planetary Data System.

Campbell, B. A., D. B. Campbell, J. L. Margot, R. R. Ghent, M. Nolan, J. Chandler, L. M. Carter, and N. J. S. Stacy (2007), Focused 70-cm wavelength radar mapping of the Moon, *IEEE Trans. Geosci. Remote Sens.*, *45*(12), 4032–4042, doi:10.1109/TGRS.2007.906582.

Campbell, B. A., L. M. Carter, B. R. Hawke, D. B. Campbell, and R. R. Ghent (2008), Volcanic and impact deposits of the Moon's Aristarchus Plateau: A new view from Earth-based radar images, *Geology*, *36*(2), 135–138, doi:10.1130/G24310A.1.

Campbell, B. A., B. R. Hawke, L. M. Carter, R. R. Ghent, and D. B. Campbell (2009a), Rugged lava flows on the Moon revealed by Earth-based radar, *Geophys. Res. Lett.*, *36*, L22201, doi:10.1029/2009GL041087.

Campbell, B. A., B. R. Hawke, and D. B. Campbell (2009b), Surface morphology of domes in the Marius Hills and Mons Rümker regions of the Moon from Earth-based radar data, *J. Geophys. Res.*, *114*, E01001, doi:10.1029/2008JE003253.

Campbell, B. A., L. M. Carter, D. B. Campbell, M. Nolan, J. Chandler, R. R. Ghent, B. R. Hawke, R. F. Anderson, and K. Wells (2010), Earth-based 12.6-cm wavelength radar mapping of the Moon: New views of impact melt distribution and mare physical properties, *Icarus*, *208*, 565–573, doi:10.1016/j.icarus.2010.03.011.

Carter, L. M., B. A. Campbell, B. R. Hawke, D. B. Campbell, and M. C. Nolan (2009), Radar remote sensing of pyroclastic deposits in the southern Mare Serenitatis and Mare Vaporum regions of the Moon, *J. Geophys. Res.*, *114*, E11004, doi:10.1029/2009JE003406.

Carter, L. M., C. D. Neish, D. B. J. Bussey, P. D. Spudis, G. W. Patterson, J. T. Cahill, and R. K. Raney (2012), Initial observations of lunar impact melts and ejecta flows with the Mini-RF radar, *J. Geophys. Res.*, *117*, E00H09, doi:10.1029/2011JE003911.

Carter, L. M., C. D. Neish, G. W. Patterson, D. B. J. Bussey, J. T. S. Cahill, M. C. Nolan, B. J. Thomson, and The Mini-RF Team (2014), The Mini-RF Radar: Polarization performance and comparison with prior radar data, 45th *Lunar Planet. Sci. Conf.*, abstract 2152, Houston, Tex.

Drozd, R. J., C. M. Hohenberg, C. J. Morgan, F. A. Podosek, and M. L. Wroge (1977), Cosmic-ray exposure history at Taurus-Littrow, *Proc. Lunar Sci. Conf.*, *8*, 3027–3043.

Fa, W., and Y. Cai (2013), Circular polarization ratio characteristics of impact craters from Mini-RF observations and implications for ice detection at the polar regions of the Moon, *J. Geophys. Res. Planets*, *118*, 1582–1608, doi:10.1002/jgre.20110.

Fa, W., and M. A. Wieczorek (2012), Regolith thickness over the lunar nearside: Results from Earth-based 70-cm Arecibo radar observations, *Icarus*, *218*(2), 771–787, doi:10.1016/j.icarus.2012.01.010.

Fa, W., M. A. Wieczorek, and E. Heggy (2011), Modeling polarimetric radar scattering from the lunar surface: Study on the effect of physical properties of the regolith layer, *J. Geophys. Res.*, *116*, E03005, doi:10.1029/2010JE003649.

Gaddis, L. R., C. M. Pieters, and B. R. Hawke (1985), Remote sensing of lunar pyroclastic mantling deposits, *Icarus*, *61*, 461–489.

Gaddis, L. R., P. J. Mouginis-Mark, R. Singer, and V. Kaupp (1989), Geologic analyses of Shuttle Imaging Radar (SIR-B) data of Kilauea volcano, Hawaii, *Geol. Soc. Am. Bull.*, *101*, 317–322.

Gaddis, L. R., P. J. Mouginis-Mark, and J. N. Hayashi (1990), Lava flow surface textures: SIR-B radar image texture, field observations, and terrain measurements, *Photogramm. Eng. Remote Sens.*, *56*(2), 211–224.

Gaddis, L. R., M. I. Staid, J. A. Tyburczy, B. R. Hawke, and N. E. Petro (2003), Compositional analyses of lunar pyroclastic deposits, *Icarus*, *161*, 262–280, doi:10.1016/S0019-1035(02)00036-2.

Gault, D. E., and J. A. Wedekind (1969), The destruction of tektites by micrometeoroid impact, *J. Geophys. Res.*, *74*(27), 6780–6794, doi:10.1029/JB074i027p06780.

Gault, D. E., W. L. Quaide, V. R. Oberbeck, and H. J. Moore (1966), Luna 9 photographs: Evidence for a fragmental surface layer, *Science*, *153*, 985–988.

Glotch, T. D., et al. (2010), Highly silicic compositions on the Moon, *Science*, *329*, 1510–1513, doi:10.1126/science.1192148.

Glotch, T. D., J. J. Haggerty, P. G. Lucey, B. R. Hawke, T. A. Giguere, J. A. Arnold, J.-P. Williams, B. L. Jolliff, and D. A. Paige (2011), The Mairan domes: Silicic volcanic constructs on the Moon, *Geophys. Res. Lett.*, *38*, L21204, doi:10.1029/2011GL049548.

Greenhagen, B. T., et al. (2010), Global silicate mineralogy of the Moon from the Diviner Lunar Radiometer, *Science*, *329*, 1507–1509, doi:10.1126/science.1192196.

Head, J. W. (1974), Lunar dark-mantle deposits: Possible clues to the distribution of early mare deposits, *Proc. Fifth Lunar Sci. Conf., Geochim. Cosmochim. Acta*, Suppl. 5, 1, 207–222.

Head, J. W., and T. B. McCord (1978), Imbrian-age highland volcanism on the Moon: The Gruithuisen and Mairan domes, *Science*, *199*(4336), 1433–1436, doi:10.1126/science.199.4336.1433.

Heather, D. J., S. K. Dunkin, and L. Wilson (2003), Volcanism on the Marius Hills plateau: Observational analyses using Clementine multi-spectral data, *J. Geophys. Res.*, *108*(E3), 5017, doi:10.1029/2002JE001938.

Hörz, F., E. Schneider, D. E. Gault, J. B. Hartung, and D. E. Brownlee (1975), Catastrophic rupture of lunar rocks: A Monte Carlo simulation, *Moon*, *13*, 235–258.

Huang, J., L. Xiao, L. He, L. Qiao, J. Zhao, and H. Li (2011), Geological characteristics and model ages of Marius Hills on the Moon, *J. Earth Sci.*, *22*(5), 601–609, doi:10.1007/s12583-011-0211-8.

Kiefer, W. S. (2013), Gravity constraints on the subsurface structure of the Marius Hills: The magmatic plumbing of the largest lunar volcanic dome complex, *J. Geophys. Res. Planets*, *118*, 733–745, doi:10.1029/2012JE004111.

Kreslavsky, M. A., J. W. Head, G. A. Neumann, M. A. Rosenburg, O. Aharonson, D. E. Smith, and M. T. Zuber (2013), Lunar topographic roughness maps from Lunar Orbiter Laser Altimeter (LOLA) Data: Scale dependence and correlation with geologic features and units, *Icarus*, doi:10.1016/j.icarus.2013.04.027.

Lawrence, S. J., et al. (2013), LRO observations of morphology and surface roughness of volcanic cones and lobate lava flows in the Marius Hills, *J. Geophys. Res. Planets*, *118*, 615–634, doi:10.1002/jgre.20060.

Neumann, G. A., J. B. Abshire, O. Aharonson, J. B. Garvin, X. Sun, and M. T. Zuber (2003), Mars Orbiter Laser Altimeter pulse width mea-surements and footprint-scale roughness, *Geophys. Res. Lett.*, *30*(11), 1561, doi:10.1029/2003GL017048.

Neumann, G. A., D. E. Smith, M. T. Zuber, E. Mazarico, M. H. Torrence, J. C. Cavanaugh, and LOLA Science Team (2009), Meter-scale roughness on the Moon from Lunar Orbiter Laser Altimeter (LOLA) pulse spreading: Implications for exploration, paper presented at the Annual Meeting of the Lunar Exploration Analysis Group, Lunar and Planet. Inst., Houston, Tex.

Nozette, S., et al. (2010), The lunar reconnaissance orbiter miniature radio frequency (Mini-RF) technology demonstration, *Space Sci. Rev.*, *150*, 285–302, doi:10.1007/s11214-009-9607-5.

Pettengill, G. H., and T. W. Thompson (1968), A radar study of the lunar crater Tycho at 3.8-cm and 70-cm wavelengths, *Icarus*, *8*, 457–471.

Plaut, J. J., S. W. Anderson, D. A. Crown, E. R. Stofan, and J. J. van Zyl (2004), The unique radar properties of silicic lava domes, *J. Geophys. Res.*, *109*, E03001, doi:10.1029/2002JE002017.

Poole, W. D., J.-P. Muller, and S. Gupta (2013), How reliable are surface roughness estimates from planetary laser altimeter pulse widths? An assessment using MOLA and LOLA pulse-width data, 44th *Lunar Planet. Sci. Conf.*, abstract 1511, Houston, Tex.

Prettyman, T. H., J. J. Hagerty, R. C. Elphic, W. C. Feldman, D. J. Lawrence, G. W. McKinney, and D. T. Vaniman (2006), Elemental composition of the lunar surface: Analysis of gamma ray spectroscopy data from Lunar Prospector, *J. Geophys. Res.*, *111*, E12007, doi:10.1029/2005JE002656.

Quaide, W., and V. Oberbeck (1975), Development of the mare regolith: Some model considerations, *Moon*, *13*, 27–55.

Raney, R. K., et al. (2011), The lunar Mini-RF radars: Hybrid polarimetric architecture and initial results, *Proc. IEEE*, *99*(5), 808–823, doi:10.1109/JPROC.2010.2084970.

Rosenburg, M. A., O. Aharonson, J. W. Head, M. A. Kreslavsky, E. Mazarico, G. A. Neumann, D. E. Smith, M. H. Torrence, and M. T. Zuber (2011), Global surface slopes and roughness of the Moon from the Lunar Orbiter Laser Altimeter, *J. Geophys. Res.*, *116*, E02001, doi:10.1029/2010JE003716.

Saran, S., A. Das, S. Mohan, and M. Chakraborty (2012), Study of scattering characteristics of lunar equatorial region using Chandrayaan-1 Mini-SAR polarimetric data, *Planet. Space Sci.*, *71*, 18–30, doi:10.1016/j.pss.2012.06.014.

Shepard, M. K., B. A. Campbell, M. H. Bulmer, T. G. Farr, L. R. Gaddis, and J. J. Plaut (2001), The roughness of natural terrain: A planetary and remote sensing perspective, *J. Geophys. Res.*, *106*(E12), 32,777–32,795, doi:10.1029/2000JE001429.

Smith, D. E., et al. (2010a), Initial observations from the Lunar Orbiter Laser Altimeter (LOLA), *Geophys. Res. Lett.*, *37*, L18294, doi:10.1029/2010GL043751.

Smith, D. E., et al. (2010b), The lunar orbiter laser altimeter investigation on the lunar reconnaissance orbiter, *Space Sci. Rev.*, *150*, 209–241, doi:10.1007/s11214-009-9512-y.

Soderblom, L. A. (1970), A model for small-impact erosion applied to the lunar surface, *J. Geophys. Res.*, *75*(14), 2655–2661, doi:10.1029/JB075i014p02655.

Spudis, P. D., et al. (2010), Initial results for the north pole of the Moon from Mini-SAR, Chandrayaan-1 mission, *Geophys. Res. Lett.*, *37*, L06204, doi:10.1029/2009GL042259.

Spudis, P. D., et al. (2013), Evidence for water ice on the Moon: Results for anomalous polar craters from the LRO Mini-RF imaging radar, *J. Geophys. Res. Planets*, *118*, 2016–2029, doi:10.1002/jgre.20156.

Sunshine, J. M., C. M. Pieters, and J. W. Head (1994), New evidence for compositional diversity on the Marius Hills plateau from *Galileo* multispectral imaging, 25th *Proc. Lunar Planet. Sci. Conf.*, 1359–1360, Houston, Tex.

Thompson, T. W., E. A. Ustinov, and E. Heggy (2011), Modeling radar scattering from icy lunar regoliths at 13 cm and 4 cm wavelengths, *J. Geophys. Res.*, *116*, E01006, doi:10.1029/2009JE003368.

Thomson, B. J., et al. (2012), An upper limit for ice in Shackleton crater as revealed by LRO Mini-RF orbital radar, *Geophys Res Lett*, *39*, L14201, doi:10.1029/2012GL052119.

Wagner, R., J. W. Head III, U. Wolf, and G. Neukum (2002), Stratigraphic sequence and ages of volcanic units in the Gruithuisen region of the Moon, *J. Geophys. Res.*, *107*(E11), 5104, doi:10.1029/2002JE001844.

Weitz, C. M., and J. W. Head (1999), Spectral properties of the Marius Hills volcanic complex and implications for the formation of lunar domes and cones, *J. Geophys. Res.*, *104*(E8), 18,933–18,956, doi:10.1029/1998JE000630.

Weitz, M., J. W. Head, and C. M. Pieters (1998), Lunar regional dark mantle deposits: Geologic, multispectral, and modeling studies, *J. Geophys. Res.*, *103*(E10), 22,725–22,759, doi:10.1029/98JE02027.

Whitford-Stark, J. L., and J. W. Head (1980), Stratigraphy of Oceanus Procellarum basalts: Sources and styles of emplacement, *J. Geophys. Res.*, *85*, 6579–6609, doi:10.1029/JB085iB11p06579.

Wilhelms, D. E. (1987), *The Geologic History of the Moon*, *U.S. Geol. Surv. Prof. Pap.*, *1348*, 302 pp.

Wilson, L., and J. W. Head (1981), Ascent and eruption of basaltic magma on the Earth and Moon, *J. Geophys. Res.*, *86*(B4), 2971–3001, doi:10.1029/JB086iB04p02971.

Wilson, L., and J. W. Head (2003), Lunar Gruithuisen and Mairan domes: Rheology and mode of emplacement, *J. Geophys. Res.*, *108*(E2), 5012, doi:10.1029/2002JE001909.

Zisk, S. H., G. H. Pettengill, and G. W. Catuna (1974), High-resolution radar maps of the lunar surface at 3.8-cm wavelength, *Moon*, *10*, 17–50, doi:10.1007/BF00562017.